# Differential spatial regulation and activation of integrin nanoclusters inside focal adhesions.

Sarah Keary[1], Nicolas Mateos[1], Felix Campelo[1], and Maria F. Garcia-Parajo[1,2,*]

[1] *ICFO – Institut de Ciencies Fotoniques, The Barcelona Institute of Science and Technology, 08860 Castelldefels (Barcelona), Spain.*

[2] *ICREA, Pg. Lluís Companys 23, 08010 Barcelona, Spain.*

**Corresponding author:**

* Maria F. Garcia-Parajo: maria.garcia-parajo@icfo.eu

**Author Contributions:** S.K prepared the biological samples, performed STORM imaging and analyzed the data. N.M. developed algorithms for data analysis and contributed to the analysis. F.C. and M.F.G.-P. supervised the research. S.K., F.C. and M.F.G.-P conceived and discussed the experiments, interpreted the data, and wrote the paper.

**Competing Interest Statement:** The authors declare no competing interests.

**Classification:** Major: Biological Sciences. Minor: Biophysics and Computational Biology.

**Keywords:** Adhesion proteins, receptor nanoclustering, super-resolution STORM microscopy, mechanobiology, integrin activation.

**This PDF file includes:**

Main Text
Figures 1 to 5

**Abstract**

$\alpha_5\beta_1$ and $\alpha_v\beta_3$ integrins are key components of focal adhesions (FAs) that play important roles in cell adhesion, migration and mechanobiology-dependent processes. Whether both integrins work in concert or their activities are differentially regulated inside FAs is not fully understood. Here, we exploited dual-color super-resolution stochastic optical reconstruction microscopy (STORM) to quantitatively assess the lateral nanoscale organization and activation state of both integrins and main adaptors inside FAs. Our results reveal that key FA proteins $\alpha_5\beta_1$, $\alpha_v\beta_3$, paxillin, talin and vinculin organize into segregated nanoclusters of similar size (~50 nm) and number of molecules, regardless of their partitioning in the membrane, confirming that integrin nanoclustering is force-independent. Both integrins further segregate as active or inactive nanoclusters that do not intermix at the nanoscale and with a higher fraction of active $\alpha_5\beta_1$ nanoclusters as compared to $\alpha_v\beta_3$. We find a nearly 1:1 stoichiometry between active integrin and adaptor nanoclusters indicating that coordinated integrin nanocluster activation occurs via the concurrent engagement of talin and vinculin nanoclusters. Interestingly, active $\alpha_5\beta_1$ nanoclusters preferentially localize at the FA periphery in proximity to paxillin, talin and vinculin nanoclusters, establishing multiprotein nano-hubs, whereas $\alpha_v\beta_3$ nanoclusters uniformly distribute throughout FAs. Overall, we reveal a highly complex lateral organization of integrins and main adaptors within FAs, where adhesion proteins arrange as modular nanoscale units that distinctively organize inside FAs to spatially regulate integrin activation. Such spatial control of integrin activity provides a physical mechanism to tune their functions having implications for their key roles in physiology and disease.

45 **Significance Statement**

46 Focal adhesions (FAs) are places for cell attachment to the extracellular matrix that influence
47 multiple cellular processes as well as being sites for sensing and transducing mechanical
48 stimuli. Integrins, core components of FAs, have different activation states and execute
49 diversity of functions, but how their activity and roles are regulated remain mysterious. Using
50 quantitative dual-color super-resolution microscopy we reveal that integrin activation is
51 spatially regulated inside FAs. We show that main adhesion proteins organize as universal
52 modular nanoscale units, spatially segregating from each other inside FAs. Remarkably, these
53 modular units distinctively organize inside FAs selectively activating one type of integrin or
54 another at specific locations within FAs, providing a physical mechanism to regulate integrin
55 activation and possibly function.

56

57 **Main Text**

58 **Introduction**

59 Adhesion complexes (ACs) in adherent cells, such as focal adhesions (FAs) and fibrillar
60 adhesions (fAs) are places for cell attachment, mechanosensing and mechanotransduction (1–
61 4). These structures are composed by different integrin receptors that bind to their ligands on
62 the extracellular matrix (ECM), and by a myriad of intracellular protein adaptors that
63 dynamically connect integrins to the actin cytoskeleton machinery relaying the transmission of
64 mechanical forces in a bidirectional manner (5–7). Studies over the last two decades have
65 provided a wealth of information focused on understanding these complexes, the proteins they
66 contain, their role in mechanosensing and in cellular processes such as migration and
67 proliferation as well as on how influential their regulation is in developmental and pathogenic
68 processes (8–15).

69 Integrins $\alpha_5\beta_1$ and $\alpha_v\beta_3$ are transmembrane heterodimeric proteins critical for the formation of
70 ACs. Both $\alpha_5\beta_1$ and $\alpha_v\beta_3$ bind to the RGD peptide motif of certain ECM components, such as
71 fibronectin (16–18), and are linked to the cell's cytoskeleton via many of the same adaptor
72 proteins (19–24). The apparent redundancy of different integrins binding to the same ligand
73 and same adaptor proteins is intriguing and has been the subject of intense research over the
74 past years. Earlier studies on primary fibroblasts showed that these integrins segregate in
75 different adhesion structures, indicating different roles, with $\alpha_5\beta_1$ being enriched in fAs (25),
76 adhesive sites at central regions of the cell, and $\alpha_v\beta_3$ being confined to focal complexes at the
77 base of cellular protrusions, and to FAs, which anchor contractile stress fibers at the periphery
78 of the cell (26). However, more recent super-resolution microscopy studies showed that both
79 types of integrins are simultaneously present inside FAs (27). In vitro reconstitution
80 experiments suggested that $\alpha_5\beta_1$ determines adhesion strength because its catch-bond binding
81 to fibronectin and rupture force to its ligand is higher (~10–30 pN) than that of $\alpha_v\beta_3$ (~5–25
82 pN) (28, 29). Moreover, the lower bond strength of $\alpha_v\beta_3$ coupled to its faster binding and
83 unbinding rates suggests a possible role for $\alpha_v\beta_3$ in mechanosensing (5). Nevertheless, single
84 molecule tracking data indicated that $\alpha_v\beta_3$ integrins are mainly stationary inside FAs and more
85 stably bound to the ligand, favoring adhesion as its main role (27). It has been also shown that
86 $\alpha_5\beta_1$ is involved in Rho activation during late spreading, enhancing RhoA-mediated

87 actomyosin contractility (26, 30), supporting the idea that $\alpha_5\beta_1$ is involved in force-mediated
88 adhesion reinforcement. In a *tour-de-force* effort, Fässler and colleagues found that only the
89 simultaneous expression of both integrins enabled cells to sense the rigidity of the ECM and to
90 respond by reinforcing the actomyosin structure (31). These results, supported by others (32),
91 have led to the recent notion that both integrins work in a synergistic manner, exhibiting
92 cooperativity during cell adhesion, migration and mechanosensing, although the mechanisms
93 are far from being fully resolved (32).

94 The highly dynamic conformational states exhibited by integrins together with their lateral and
95 axial nanoscale organization might play important roles regulating the differential or
96 synergistic functions of different integrins inside FAs. Indeed, it has been shown that integrins
97 can rapidly transition between different conformational states that relate to their activation and
98 binding capacity to their ligands (27, 33, 34). Moreover, in addition to the nanoscale axial
99 segregation of different AC components inside FAs (35), it has been reported that integrins as
100 well as different adaptor proteins also segregate laterally into small nanoclusters inside FAs
101 (36–39). Recent super-resolution studies have further shown that $\alpha_5\beta_1$ segregates in both active
102 and inactive nanoclusters inside FAs (38) and single-molecule tension measurements
103 uncovered distinct sub-populations of load-bearing integrins and a high fraction of unengaged
104 integrins (40, 41). Together, these results suggest that at any given time only a fraction of
105 integrins might be active inside FAs and engaged with their adaptor partners. Such a dynamic
106 scenario would allow integrins to differentially interact with their environment and possibly
107 diversify their functions. As $\alpha_5\beta_1$ and $\alpha_v\beta_3$ have different activation states and are both
108 contained in FAs, it is plausible that their spatial regulation and activation state inside FAs
109 provides a physical mechanism to tune their functions. However, such studies have not been
110 reported yet.

111 Here, we combined dual-color super-resolution microscopy together with robust analytical
112 tools to study a number of endogenous FA proteins on human fibroblast cells. Specifically, we
113 imaged one of the two integrins ($\alpha_5\beta_1/\alpha_v\beta_3$), their full population or active conformations, with
114 each of three key adaptors proteins, paxillin, talin and vinculin. Our results show that all of
115 these proteins form segregated nanoclusters of remarkably similar size and molecular density
116 inside FAs, and also outside ACs. Moreover, we find sub-populations of active and inactive

117 $\alpha_5\beta_1$ and $\alpha_v\beta_3$ nanoclusters inside FAs, which spatially segregate from each other and provide
118 evidence for a nearly 1:1 stoichiometry between talin, vinculin and active integrin nanoclusters.
119 Interestingly, whereas $\alpha_v\beta_3$ nanoclusters organize randomly inside FAs regardless of their
120 activation state, active $\alpha_5\beta_1$ nanoclusters preferentially organize at the edges of FAs. Overall,
121 we propose that the nano- and meso-scale organization of $\alpha_5\beta_1$ and $\alpha_v\beta_3$ integrins and their
122 distinct lateral segregation and activation state are key factors in the differentiation of their
123 roles within FAs.

124

125 **Results**

126 **Proteins of the ACs organize as universal nanoclusters across regions of the basal**
127 **membrane.**

128 We employed dual-color super-resolution microscopy based on stochastic optical
129 reconstruction microscopy (STORM) to determine how adhesion proteins (integrins and key
130 adaptor proteins) are spatially organized at the nanoscale. Human fibroblasts (HFF-1 cells)
131 were seeded on fibronectin (FN)-coated glass slides for 24 h, after which the cells were
132 processed for immunofluorescence, where one integrin heterodimer ($\alpha_5\beta_1$ or $\alpha_v\beta_3$, targeting
133 either the total or the active integrin population) together with one adaptor protein (paxillin, C
134 terminus of talin-1, or vinculin) were labeled and imaged using STORM. Given the huge
135 number of adaptor proteins that have been reported to interact with integrins (19, 21), we chose
136 for paxillin, talin and vinculin since they belong to the core-components of the adhesome (23)
137 and crucially locate at distinct axial layers of functional activity, i.e., paxillin at the signaling
138 layer, while talin and vinculin locate at the force-transduction layer (35).

139 Super-resolution images qualitatively revealed an inhomogeneous distribution for all the
140 proteins examined, forming small and laterally segregated nanoclusters inside FAs (Fig. 1A–
141 D). To quantitatively substantiate these observations, we first used a mask to classify all the
142 single molecule localization events according to their location on the membrane, i.e., FAs, fAs
143 or outside ACs (see Materials & Methods, Fig. S1A-F). We then used the STORM-compatible
144 density-based spatial clustering of applications with noise (DBSCAN) algorithm (42) to group
145 localizations into nanoclusters (see Materials & Methods). Because STORM data consists of
146 lists of single-molecule localizations and each labeled protein can be localized multiple times
147 (43), we used the distribution of the number of localizations obtained from isolated fluorescent

148 spots on glass, mostly corresponding to individual antibodies (Abs), to establish a threshold for
149 the minimum number of localizations per cluster (38, 44), ensuring that what we consider
150 nanoclusters indeed contain multiple proteins (Fig. 1E, see Materials & Methods). DBSCAN
151 classified between 70% to 80% of the localizations of each of the proteins as belonging to
152 nanoclusters, regardless of whether they were located inside FAs or on regions of the
153 membrane outside adhesions (Fig. S1G-I). Notably, the number of localizations per nanocluster
154 and their size were similar across the different adhesion proteins (integrins and adaptors) inside
155 FAs, with a median of ~20 localizations per nanocluster, likely corresponding to a few copies
156 of the protein, and a diameter of ~40–45 nm (Fig. 1F,G). Similar results in terms of size and
157 number of localizations per nanocluster were obtained when performing the analysis outside
158 ACs (Fig. S2). In addition, the nanocluster characteristics were maintained when specifically
159 labeling the active integrin ($\alpha_5\beta_1$ or $\alpha_v\beta_3$) populations (Fig. 1D,F,G). These results are in good
160 quantitative agreement with previous reports showing that both active and inactive integrin
161 $\alpha_5\beta_1$ nanoclusters have a median size of 40 nm and 35 nm, respectively (38). Overall, our results
162 show that $\alpha_5\beta_1$ and $\alpha_v\beta_3$ integrin receptors as well as their main adaptor proteins, paxillin, talin
163 and vinculin, form laterally segregated nanoclusters of similar size and number of molecules.
164 Interestingly, such nanoscale organization is independent of whether these adhesion proteins
165 partition inside FAs or outside ACs (Fig. S2).

166 **Global mesoscale organization of adhesion protein nanoclusters inside FAs.**

167 We next sought to investigate how the different adhesion proteins laterally organize inside FAs
168 beyond their nanoclustering, i.e., at the mesoscale. For this, we first quantified the density of
169 nanoclusters per unit area of the membrane, within FAs (Fig. 2A) and outside ACs (Fig. 2B).
170 As expected, the density of nanoclusters was larger in FAs as compared to outside adhesions
171 (~5–10 fold increase) (Fig. 2A,B). Because adaptor proteins, such as talin or vinculin, are
172 shared between $\alpha_5\beta_1$ and $\alpha_v\beta_3$ integrins (23), we compared the density of the full population of
173 integrin nanoclusters (~36 $\mu m^{-2}$ in FAs) to the density of adaptor protein nanoclusters (~10–12
174 $\mu m^{-2}$ for talin and vinculin, ~20 $\mu m^{-2}$ for paxillin in FAs). These data reveal a significantly
175 higher (~2–4 fold) density of integrin nanoclusters in comparison to their adaptors and,
176 consequently, a stoichiometric mismatch between the integrins and the adaptors, regardless of
177 whether they partition inside or outside FAs (Fig 2A,B). Since the active integrin conformation
178 is the one engaged with the adaptors (45, 46), we also quantified the density of active integrin

179 nanoclusters per unit area. Notably, the density of active integrin nanoclusters inside FAs was
180 considerably smaller than that of the full population (~ 30% less in the case of act$\beta_1$ and ~ 20%
181 less for act$\beta_3$) (Fig. 2A), indicating that at any given time there is a large percentage of inactive
182 integrin nanoclusters inside FAs. Notably, the total density of active $\alpha_5\beta_1$ and $\alpha_v\beta_3$ integrin
183 nanoclusters stoichiometrically matches that of talin and vinculin nanoclusters, and it is only
184 slightly outnumbered by paxillin nanoclusters inside FAs (Fig. 2A), suggesting that these active
185 integrins might be fully engaged to their adaptors. The modest percentage of active $\alpha_5\beta_1$
186 integrin nanoclusters observed in our data (~ 30%, Fig. 2A) is in agreement with a recent report
187 from Spiess *et al*, obtained using a different super-resolution technique (38) and consistent with
188 the high percentage of low-force bearing integrins measured by using single-molecule force
189 sensors (41). In addition to the $\alpha_5\beta_1$ results, our data also reveal the existence of a sub-
190 population of $\alpha_v\beta_3$ active nanoclusters inside FAs (Fig. 2A). Moreover, active and inactive $\alpha_v\beta_3$
191 integrins most probably segregate in different nanoclusters, as the number of integrins and size
192 of active $\alpha_v\beta_3$ nanoclusters are similar to that of their total population (Fig. 1F,G). Together,
193 these results enforce the notion of a coordinated mechanism that laterally segregates active and
194 inactive integrins into distinct nanoclusters that is general and common for both integrins.

195 Interestingly, despite this common feature, we found a significantly higher density of $\alpha_5\beta_1$
196 nanoclusters as compared to $\alpha_v\beta_3$ (Fig. 2A,B). Moreover, the percentage of active $\alpha_5\beta_1$ integrin
197 nanoclusters was larger than for $\alpha_v\beta_3$, in particular inside FAs (30% and 20% for active $\alpha_5\beta_1$
198 and active $\alpha_v\beta_3$, respectively) (Fig. 2A). To further enquire whether both types of integrin
199 nanoclusters would act in concert by associating together at the nanoscale sharing their vinculin
200 and talin partners, we performed dual color STORM imaging of the total populations of $\alpha_5\beta_1$
201 and $\alpha_v\beta_3$ integrins (Fig. 2C). Visual inspection as well as quantification of the images show that
202 $\alpha_5\beta_1$ and $\alpha_v\beta_3$ do not intermix at the nanoscale, forming distinct nanoclusters that spatially
203 segregate from each other inside FAs (Fig. S3A,B). The differential degree of $\alpha_5\beta_1$ and $\alpha_v\beta_3$ in
204 terms of expression, activation state, and lateral nano- and meso-scale segregation suggests a
205 potential distinct role for both types of integrins inside FAs.

206 To get a better understanding on the global organization of both types of integrins in relation
207 to their main adaptor proteins, we calculated the edge-to-edge distance between the nearest-
208 neighbor integrin nanoclusters and each of the adaptors (see Materials & Methods). Although

209 visual inspection of the dual color STORM images already suggested that integrin nanoclusters
210 are also physically segregated from their adaptor partners (Fig. 1B,C) we used this quantitative
211 approach to estimate the degree of colocalization (i.e., spatial overlap) between different
212 nanoclusters. Since we measure edge-to-edge distances between nearest nanoclusters (EED-
213 NN), values below zero correspond to physically overlapping nanoclusters, EED-NN values
214 above zero to spatially segregated nanoclusters, and EED-NN = 0 corresponds to contiguous
215 nanoclusters, i.e., next to each other. Our results quantitively confirm that the large majority of
216 $\alpha_5\beta_1$ and $\alpha_v\beta_3$ nanoclusters are laterally segregated from their adaptor partners (Fig. 2D, Fig.
217 S3C,D). Their spatial segregation is essentially determined by the density of nanoclusters
218 within the FAs, as similar EED-NN distributions were obtained from simulations of particles
219 uniformly distributed inside the experimentally obtained FAs, using identical particle densities
220 as to the ones obtained experimentally for the integrin nanoclusters and the different adaptors
221 (Materials & Methods and *SI Text 1*) (Fig. 2D, black lines). Considering the canonical view
222 that integrins inside FAs are bound to paxillin and engaged to talin and vinculin (45, 47), these
223 results might be surprising at first sight, as one would expect a much higher fraction of EED-
224 NN values below zero. Nevertheless, using super-resolution microscopy, others have also
225 found negligible spatial colocalization of integrins with these adaptor proteins (38, 39).
226 Moreover, Dunn and co-workers also found that most ligand-bound integrins inside FAs exist
227 in a minimally tensioned state (< 2 pN) and not dependent on the actin cytoskeleton (41). These
228 results are fully in line with the lack of colocalization or spatial proximity of integrins to talin
229 and vinculin as we determined here, since these two adaptors mediate the linkage of integrins
230 to the actin cytoskeleton (45, 48).

231 It has been recently proposed that adhesion proteins including integrins organize in a
232 hierarchical fashion inside FAs, forming nanoclusters similar to the ones reported here, that
233 further enrich into compartmentalized regions around 300 nm in size (39). To enquire whether
234 such hierarchical organization is present in our data, we performed nearest-neighbor distance
235 (NND) analysis between nanoclusters of the same proteins (Fig. 2E). In addition, we
236 implemented simulations of uniformly distributed particles inside the experimental FA regions,
237 using the same experimental nanoclusters densities, and made the corresponding NND analysis
238 (Fig. 2E). Notably, our results show that the global organization of all the adhesion protein
239 nanoclusters investigated is fully uniform inside FAs, as the experimental NND distributions

240 were indistinguishable from those of randomly distributed particles (Fig. 2E). Thus, in contrast
241 to earlier results (39), we do not find evidence for any particular spatial enrichment of protein
242 nanoclusters inside FAs, instead, the characteristic nanocluster separation is exclusively
243 dictated by their density inside FAs.

244 **Integrin $\alpha_5\beta_1$ but not $\alpha_v\beta_3$ nanoclusters are enriched on FA edges.**
245 Our previous analysis rendered a uniform inter-cluster organization of all adhesion protein
246 nanoclusters inside FAs. Yet, visual inspection of the dual-color STORM images suggests that
247 a significant fraction of $\alpha_5\beta_1$ nanoclusters might preferentially localize on FA edges (Fig. 1B).
248 To quantify these observations, we calculated the shortest-path distance from each $\alpha_5\beta_1$
249 nanocluster to the edge of its corresponding FA, i.e., the distance-to-FA-edge ($d2e$), and
250 generated a histogram of these values, i.e., $H_{exp}(d2e)$ (Fig. 3A). In addition, we generated a
251 similar histogram from simulations of uniformly distributed $\alpha_5\beta_1$ nanoclusters on FAs without
252 overlapping to one another, $H_{sim}(d2e)$ (see *SI Text 1*). In general, if the nanoclusters were
253 uniformly distributed throughout the FA, one would expect that the probability of finding a
254 nanocluster at a specific distance to the FA edge decreases with increasing distance. This occurs
255 because there is a larger area along the perimeter of any given shape and thus a higher number
256 of nanoclusters (e.g., for a circular shape, the decrease is linear with the distance to the FA
257 edge). We found that our experimental and simulated data indeed exhibit this general trend,
258 although, notably, a higher percentage of $\alpha_5\beta_1$ nanoclusters were detected at distances below
259 100 nm from the FA edges, as compared to a uniform distribution (Fig. 3A and *inset*), indicative
260 of their preference to locate closer to the FA edges. Similar trends were also obtained for
261 paxillin and talin (Fig. S4A,B), whereas for $\alpha_v\beta_3$ and vinculin the distributions were
262 indistinguishable from random (Fig. S4C,D).

263 To better assess the extent of nanocluster enrichment at FA edges on a cell-to-cell basis, we
264 then computed the median (*Mdn*) values of the $H_{exp}(d2e)$ obtained over many FAs per cell
265 and those corresponding to the simulated data, $H_{sim}(d2e)$, and calculated the edge-proximity-
266 factor (EPF) as the relative difference between them, i.e., EPF =
267 $\left(Mdn(H_{exp}(d2e)) - Mdn(H_{sim}(d2e))\right)/Mdn(H_{sim}(d2e))$. Hence, negative (positive) EPF
268 values indicate preferential nanocluster enrichment (depletion) at FA edges. Moreover, to
269 statistically determine whether the distribution of EPF values was different from zero (the EPF

270 value expected from a random distance to the FA edge distribution) we ran a paired Student's
271 t-test for each protein comparing the $H_{exp}(d2e)$ with the corresponding $H_{sim}(d2e)$. This
272 analysis showed that most proteins exhibit some degree of enrichment at the edges of the FAs
273 (i.e., negative EPF values), although their magnitude was markedly different amongst them
274 (Fig. 3B). The highest enrichments at the FA edges were found for the full population of $\alpha_5\beta_1$
275 nanoclusters and their active sub-population (~30% closer to the FA edge than if uniformly
276 distributed) and for talin, whereas the enrichment at the FA edges of the total $\alpha_v\beta_3$ population
277 and paxillin was much more modest. Notably, the active $\alpha_v\beta_3$ sub-population and vinculin
278 showed no preferential enrichment at the FA edges (Fig. 3B).

279 To establish the characteristic distances of protein enrichment with respect to the FA edges, we
280 next computed the difference between the experimental and simulated distributions, i.e., the
281 deviation from random, $\Delta d2e = H_{exp}(d2e) - H_{sim}(d2e)$, as a function of the distance to the
282 FA edges, for each of the examined proteins (Fig. 3C,D). Here, positive values of $\Delta d2e$
283 correspond to local nanocluster enrichment at a particular distance to the FA edge, whereas
284 negative values indicate nanocluster depletion. Our results show a clear difference between
285 both integrins, with $\alpha_5\beta_1$ nanoclusters being enriched on the edge on FAs (Fig. 3C, continuous
286 green line) whereas $\alpha_v\beta_3$ nanoclusters showed a rather uniform distribution, independently of
287 the distance to the FA edges (Fig. 3C, continuous blue line). Moreover, this preferential
288 enrichment of $\alpha_5\beta_1$ but not of $\alpha_v\beta_3$ nanoclusters at the FA edges was retained when specifically
289 analyzing the active integrin conformations (Fig. 3C, dashed green and blue lines,
290 respectively).

291 We next investigated how adaptor protein nanoclusters distribute with respect to the FA edge.
292 Similar to the results obtained for $\alpha_5\beta_1$ nanoclusters, both talin and paxillin nanoclusters
293 showed enrichment in a region between 50–150 nm from the FA edges, although somewhat
294 less pronounced as compared to $\alpha_5\beta_1$ nanoclusters (Fig. 3D), whereas vinculin nanoclusters
295 showed no preference to the FA edges. Finally, we extracted the percentage of the total and
296 active $\alpha_5\beta_1$ nanoclusters that reside within distances smaller than 100 nm from the FA edges
297 and compared the results to those from simulations of random organization (Fig. 3E). Notably,
298 a significantly larger percentage of active $\alpha_5\beta_1$ nanoclusters as compared to the total $\alpha_5\beta_1$
299 nanocluster population and to the simulations locate at the periphery of FAs (Fig. 3E).

300 Together, these results strongly indicate that integrin nanoclusters spatially organize in a rather
301 distinct fashion within FAs, with $\alpha_5\beta_1$ nanoclusters localizing preferentially at the edges of the
302 FAs and $\alpha_v\beta_3$ nanoclusters distributing randomly inside FAs. Moreover, the preferential
303 enrichment of active $\alpha_5\beta_1$ nanoclusters together with paxillin and talin at the FA edges suggests
304 that $\alpha_5\beta_1$ activation is spatially regulated inside FAs.

305 **Integrin $\alpha_5\beta_1$ forms multiprotein hubs at the FA edges**

306 Since activation of integrins involves engagement with their adaptors paxillin, talin and
307 vinculin, we sought to investigate whether the active $\alpha_5\beta_1$ nanoclusters preferentially located
308 at the FAs periphery reside in close proximity to their adaptor proteins. For this we first
309 obtained the inter-cluster NND (*i*NND) distributions between active $\alpha_5\beta_1$ nanoclusters and each
310 of the adaptor nanoclusters (Fig. S5). We calculated the *Mdn* of each *i*NND distribution and
311 used this value as a threshold to classify pairs of active $\alpha_5\beta_1$-adaptor nanoclusters as being
312 close (i.e., *i*NND < *Mdn*) or far (*i*NND > *Mdn*) from each other. Next, we separately computed
313 the distance to the FA edge ($d2e$) for the active $\alpha_5\beta_1$ nanoclusters that were found close or far
314 from their partner, and compared the results to simulated data (Fig. 4A, and *inset*). Having
315 these plots, we then calculated the deviation from random ($\Delta d2e$) as a function of the distance
316 to the FA edge, for both active $\alpha_5\beta_1$ nanoclusters close to their partner and active $\alpha_5\beta_1$
317 nanoclusters far from their partner (Fig. 4B and Fig. S6). This analysis shows that active $\alpha_5\beta_1$
318 nanoclusters preferentially partition to the FA edges regardless of their proximity to talin
319 nanoclusters (Fig. 4B) and to other adaptors (Fig. S6). Intriguingly, active $\alpha_5\beta_1$ nanoclusters
320 that are far from talin nanoclusters are still enriched at FA edges (Fig. 4B, empty green bars)
321 suggesting that other cytoplasmic adaptors, aside from talin, are able to activate $\alpha_5\beta_1$ at the FA
322 edges. Such a candidate might be tensin3, which has been recently shown to compete with talin
323 to bind $\alpha_5\beta_1$, during the formation of fAs from FAs (49). In strong contrast, active $\alpha_v\beta_3$
324 nanoclusters do not exhibit any particular preference to locate close to the FA edges regardless
325 of their proximity to talin nanoclusters, fully consistent with their random organization inside
326 FAs (Fig. 4C).

327 Finally, we enquired whether adaptor protein nanoclusters (paxillin, talin, and vinculin) close
328 to active $\alpha_5\beta_1$ nanoclusters also locate closer to the FA edges. Notably, we found that all of
329 these adaptor nanoclusters close to active $\alpha_5\beta_1$ nanoclusters are also enriched on the FA edge

330 region (~150–200 nm from the edge), whereas adaptor nanoclusters far from active $\alpha_5\beta_1$ appear
331 to be more uniformly distributed (Fig. 4D–F). Taken together, our data reveal a differential
332 mesoscale organization between active $\alpha_5\beta_1$ and $\alpha_v\beta_3$ nanoclusters inside FAs, where the
333 former preferentially form multiprotein nano-hubs together with adhesion adaptor nanoclusters
334 on the edge of FAs, and the latter organize as uniformly-distributed nanoclusters within FAs.

335 **Discussion**

336 Here, we have combined dual-color super-resolution optical microscopy together with a robust
337 set of analytical tools to provide insights on the lateral spatial organization of different adhesion
338 proteins inside FAs. Earlier reports showed that nascent adhesions (NAs) are formed due to
339 integrin nanoclusters that either rapidly disassemble at the plasma membrane without force or
340 further mature into FAs in response to mechanical forces (37, 50). Our results now show that
341 even in the presence of mechanical forces (i.e., inside FAs), integrin nanoclusters remain
342 segregated from each other while maintaining intact their sizes and number of molecules.
343 Similar integrin nanocluster properties were also found outside adhesions, reinforcing the
344 notion that integrin nanoclustering is force-independent (37). Interestingly, we found that the
345 main cytoplasmic adaptors, paxillin, talin and vinculin, also form nanoclusters of similar size
346 and number of molecules as the integrins, regardless of whether they locate inside or outside
347 FAs. Together, these results strongly indicate that adhesion proteins organize as universal
348 nano-hubs, functioning as modular adhesion units to serve multiple integrin-dependent
349 functions related to adhesion and migration but also to mechanosensing and
350 mechanotransduction.

351 Consistent with previous results (38), our data showed the co-existence of active and inactive
352 $\alpha_5\beta_1$ nanoclusters inside FAs fully segregated from each other. Remarkably, we find that $\alpha_v\beta_3$
353 shows similar functional nanoscale segregation and earlier data from our group demonstrated
354 that the integrin $\alpha_L\beta_2$ expressed on leukocytes also segregates into active and inactive
355 nanoclusters (51, 52). Thus, lateral segregation between active and inactive integrin
356 nanoclusters may represent a common feature to spatially coordinate integrin activation. How
357 could such cooperativity in integrin nanocluster activation arise? Our data shows a nearly 1:1
358 stoichiometry in the number of active integrin nanoclusters, and the main cytoplasmic adaptors
359 talin and vinculin, known to activate integrins by their engagement to the actin cytoskeleton.

360 The availability of a similar number of adaptor nanoclusters containing comparable number of
361 molecules as the integrin nanoclusters suggests that inactive integrin nanoclusters are poised
362 for their collective nanocluster activation, which is achieved upon the concurrent engagement
363 of talin and vinculin nanoclusters (and most probably also paxillin). This mechanism has been
364 shown to operate in NAs in which concurrent recruitment of talin and vinculin prior to force
365 generation is required for integrin activation and further maturation of NAs (53). In addition,
366 our data show a large percentage of $\alpha_5\beta_1$ and $\alpha_v\beta_3$ inactive integrins inside FAs and very little
367 spatial overlap between integrins and main adaptors. As integrin activation is highly dynamic
368 and transient, we propose that this pool of inactive integrin nanoclusters is required to increase
369 the probability of new engagements between integrins and their adaptors once the active
370 integrin nanoclusters become disengaged, stabilizing as a whole the FAs for lifetimes much
371 longer than the binding-unbinding dwell-times of integrins with their partners.

372 Quantification of super-resolution data revealed a higher number of $\alpha_5\beta_1$ nanoclusters
373 compared to their $\alpha_v\beta_3$ counterparts inside FAs. The relative percentage of active $\alpha_5\beta_1$
374 nanoclusters is also higher than that of $\alpha_v\beta_3$ and moreover these two integrin nanoclusters never
375 intermix inside FAs. Importantly, active $\alpha_5\beta_1$ nanoclusters preferentially locate at the periphery
376 of FAs and in close proximity with paxillin, talin and vinculin nanoclusters, while active $\alpha_v\beta_3$
377 are more uniformly distributed inside FAs. The differential degree of $\alpha_5\beta_1$ and $\alpha_v\beta_3$ in terms of
378 expression, activation state, and lateral nano- and meso-scale segregation points to a distinct
379 role for both types of integrins inside FAs, strongly indicating that integrin activation and
380 function inside FAs are spatially regulated (Fig. 5). Based on our results we postulate that *(i)*
381 $\alpha_5\beta_1$, through the ring on the FA periphery and its close proximity to paxillin, talin and vinculin
382 nanoclusters, primarily functions for substrate attachment in its high tensional state, engaging
383 with actomyosin filaments; *(ii)* $\alpha_v\beta_3$ and $\alpha_5\beta_1$ integrin nanoclusters in the central region of the
384 FA undertake the role of mechanotransduction, being more dynamic in terms of activation and
385 inactivation states and most probably engaged with shorter branched actin filaments; and *(iii)*
386 the difference in these roles is controlled by the distinct mechanical forces exerted on the
387 integrins, depending on their location inside FAs, and for $\alpha_5\beta_1$ perhaps also on its different
388 tensional states (54).

389 In summary, in contrast to the classical text book view where FAs are pictured as dense and
390 homogenous assemblies of multitude of integrins fully engaged to their cytoplasmic adaptors,
391 our work reveals a highly complex organization inside FAs, where regulation of different
392 integrins and their activation state are highly coordinated in space. We believe that such spatial
393 regulation provides the means for different integrins to synergize and/or diversify their
394 functions in terms of adhesion, migration, mechanosensing and mechanotransduction. Earlier
395 reports showed that certain proteins such as KANK1, KANK2 and $\beta_1$ integrins are enriched on
396 the edge of adhesions (55, 56) and recent data suggest that KANK1 localization around FAs is
397 driven by liquid-liquid phase separation (57). p130Cas- and FAK-dependent phase separation
398 has been also suggested to promote integrin clustering and NA assembly (58). Whether phase
399 separation also contributes to the preferential organization and activation of $\alpha_5\beta_1$ at the FA
400 edges as we reveal here is an intriguing topic that deserves further investigation.

401 **Materials and Methods**

402 **Sample preparation and immunolabeling.** HFF-1 cells (human foreskin fibroblasts) were
403 obtained from ATCC and used with low passage number (passage <15). Cells were maintained
404 in DMEM supplemented with 15% FBS and cultured in a humidified atmosphere at 37º C and
405 5% $CO_2$. Experiments were performed in cells seeded on 8-well plates (#1 Lab-Tek,
406 Thermofisher, #155411) that were previously coated with fibronectin (FN). FN coating was
407 performed by incubation with 10 µg/ml FN for 30 min at room temperature (RT). After seeding,
408 cells were allowed to spread for 24 h at 37º C and 5% $CO_2$, after which they were fixed by
409 using 4% PFA in PBS for 15 min at RT. Cells were permeabilized using 0.1% Triton X-100 in
410 PBS for 10 min and blocked with 3% BSA in PBS for 40 min. Primary antibodies against
411 integrins $\alpha_5\beta_1$ and $\alpha_v\beta_3$ –total population or specific for the active conformation–, and total
412 populations of adaptor proteins, paxillin, talin (C-terminal epitope), or vinculin, were diluted
413 in blocking buffer and added to the cells for 30 min at RT. After washing with PBS, secondary
414 antibodies that were conjugated in-house with dye pairs Alexa Fluor 405-Alexa Fluor 647 (405-
415 647 channel) or Cy3B-Alexa Fluor 647 (Cy3-647 channel), were added to the cells for 30 min
416 at RT (see Tables S1-S3 for details on reagents and antibodies used). After washing with PBS,
417 cells were stored in PBS until imaged.

418 **Image acquisition.** STORM data were obtained on a commercial Nikon Eclipse Ti system (N-
419 STORM), equipped with a 100x oil objective with NA 1.49 using TIRF illumination. The
420 detector was an ANDOR technology EMCCD iXon 897 camera, with a 256x256 pixel ROI
421 and a pixel size of 160 nm. The system has an Agilent technologies laser box with wavelengths
422 of 405 nm, 560 nm and 647 nm. STORM was performed by incubating cells in an imaging
423 buffer containing 100 mM of the reducing agent cysteamine mercaptoethylamine (MEA) (77
424 mg of MEA in 1 ml of 360 mM HCl, stock solution 1 M), the enzymatic oxygen scavenger
425 Glox solution (0.5 mg/ml glucose oxidase, 40 μg/ml catalase), and 6.25% glucose in PBS.
426 Details of the STORM imaging buffer reagents are found in Table S4. Dual color imaging was
427 carried out cyclically and sequentially. In brief, we first detected the 405-647 channel in a 5-
428 frame cycle consisting of 1 activator frame (405 nm laser on) followed by 4 reporter frames
429 (647 nm laser on), followed by the Cy3-647 channel detection sequence, similarly composed
430 of 1 activator frame (560 nm laser on) followed by 4 reporter frames (647 nm laser on). The
431 frame rate was 50 Hz (20 ms per frame) for all frames. Imaging was carried out by cyclically
432 repeating this 10-frame sequence until all the reporter dyes were exhausted (typically ~70,000
433 frames).

434 **Single molecule detection, localization precision, and STORM image reconstruction.**
435 Dual-color STORM image reconstruction was done using Insight3 software, provided by Bo
436 Huang (UCSF, initially developed in Xiaowei Zhuang's lab, Harvard University). In each
437 imaging frame, individual molecules were identified using intensity thresholding (gray levels
438 set between 600-60,000), then each intensity profile was fitted with a 2D Gaussian function to
439 identify the central position, i.e., the coordinates that represent the spatial localization of that
440 fluorescent molecule. The analysis was run over the entirety of each data set, resulting in a final
441 output that is a list of x,y coordinates (localizations) corresponding to each individual molecule
442 that has been identified. Insight3 software allows for drift correction using the correlated
443 function of the image, for details see (59). In this multi-color imaging scheme, the main source
444 of crosstalk is the nonspecific activation of the Alexa 647 by the 647 nm laser (60), which is
445 activator-independent and can occur in any frame. We implemented statistical crosstalk
446 correction where the Insight3 software analyses the full image in 50x50 nm regions of interest
447 (ROIs) and determines if each ROI is predominantly one color of the other. Based on the
448 acquisition design (in our case, one activator frame followed by four reporter frames) the

449 software determines the probability of detecting a nonspecific reporter molecule (60). To
450 minimize color cross-talk, only those localizations detected in the second frame of each five-
451 frame STORM imaging cycle (that is, the first of the four reporter frames) were considered for
452 future analytical steps. Since each single molecule can experience numerous blinking events,
453 the variation of the x,y coordinates from frame to frame determines the effective resolution
454 (61). To measure this, we detected multiple localization events arising from individual
455 molecules deposited on glass and calculated the standard deviation of the localization positions.
456 We measured the effective resolution of our system to be ~15 nm.

457 **Generation of masks and classification of the localizations belonging to FAs, fAs or**
458 **outside adhesions.** A Fiji plugin, developed by the Lakadamyali lab, was implemented as an
459 initial step to split the localization data from the STORM images into separate data sets
460 corresponding to the localizations contained in certain ROIs (62). First, the data from the two
461 channels of the reconstructed STORM image were imported and the localizations rendered
462 together in a 1024x1024 pixels image (Fig. S1A). Next, we applied an intensity threshold, until
463 the adhesion areas were visually detected, a Gaussian blur of the image (by 2 pixels), and a
464 second threshold filter until a smooth binary mask was obtained (Fig. S1B). The final mask
465 retaining only the adhesion areas was obtained by manually selecting the regions corresponding
466 to the adhesion complexes (identified by visual inspection based on their size and location). In
467 the first steps, this Fiji plugin creates separate files containing the localizations that fall within
468 the selected ROIs: all adhesions, glass, and outside adhesions (i.e., cell membrane that contain
469 the remaining areas of the image that do not correspond to all adhesions or glass). In a second
470 step the "all adhesions" file was again analyzed by the same plugin and all adhesions were split
471 into FAs and fAs and rendered with Insight3. Fig. S1C-F shows the resulting rendered
472 localizations for the different regions. These final two-color files for different cell regions were
473 then individually and independently analyzed.

474 **Image analysis.** *Clustering detection using the DBSCAN algorithm.* DBSCAN is a density-
475 based data clustering algorithm designed to be executed on arbitrary data sets with minimal
476 input from the user (42). The algorithm works by identifying arbitrary-shaped clusters of data
477 points using two user-defined input values: epsilon (eps), which is a radial distance that serves
478 to define a local neighborhood from a randomly selected initial data point; and $N_{min}$, which is
479 the minimum number of points required to be within the initial point's neighborhood so it is

480 considered part of the cluster seed. For our image analysis, spots on glass outside the cell
481 regions were analyzed using eps=20 nm and $N_{min}$=2, in order to define a minimum threshold
482 for the number of localizations per nanocluster. Important to note that we carried out this
483 analysis on glass areas found in all of our STORM images. In this way we ensure having the
484 same imaging conditions for in-cell nanoclusters and for spots-on-glass, however, at the
485 expense of having a broader distribution of localization per spot-on-glass due to the presence
486 of cell debris on the glass. When analyzing the nanoclusters found in ROIs within the cell, the
487 DBSCAN parameters were set to eps=20 nm and $N_{min}$=3 localizations, which are common
488 values used in the field (38, 44). Nevertheless, to avoid any overestimation on the degree of
489 clustering, we only considered true nanoclusters as those containing 10 or more localizations.
490 Examples on the identification of different nanoclusters by DBSCAN are shown in Fig. S1G.
491 The algorithm also provides the center of mass (CoM) coordinates of each nanocluster together
492 with the number of localizations per nanocluster and their diameter.

493 *Nearest neighbor distance (NND) analysis.* To establish how the protein nanoclusters are
494 distributed relative to one another, we used the MATLAB (MathWorks) function *knnsearch*.
495 This function computes for each nanocluster the NND, which is the shortest distance from the
496 CoM of a given nanocluster to its closest CoM nanocluster neighbor. We also used the same
497 function to determine the *i*NND (i.e., NND between nanoclusters of different proteins). To
498 measure the percentage of nanoclusters that overlap (colocalization fraction), we first
499 computed the edge-to-edge distance between nearest neighbors (EED-NN) by subtracting from
500 the NND the radii of the two-corresponding near-neighbor nanoclusters. From the EED-NN
501 distributions we calculated the percentage of occurrences with EED-NN values below zero.
502 The *knnsearch* function was also used to extract the distance-to-the-FA edge ($d2e$), i.e., the
503 shortest distance between nanoclusters and the edge of adhesions. To that end, we computed
504 the NND between the CoM of each nanocluster to the center coordinates of the list of pixels
505 that fall on the edge of the FA mask.

506 **Computational generation of uniform nanocluster distributions.** To assess whether the
507 distance distributions obtained from the experimental data (NND, EED-NN and d2e),
508 correspond to a preferential type of organization or to a uniform distribution, we performed
509 simulations by generating in silico histograms of uniformly distributed nanoclusters inside
510 FAs. In order to generate a random, uniform distribution of non-overlapping nanoclusters

within an adhesion, we first extracted the exact number and size of nanoclusters per adhesion from the experimental data and secondly, the same number of nanoclusters were randomly distributed in a uniform fashion within the adhesions, while accounting for their size and excluding any spatial overlap on nanoclusters of the same protein. A detailed description of how these in silico data sets were generated is presented in *SI Text 1* and Fig. S7.

**Statistical analysis.** Statistical analysis was carried out using GraphPad Prism (version 9.12). The details of the individual statistical tests as well as the level of significance along with p-values are explicitly provided in the figure legends. No predetermined statistical method was employed for establishing the sample size, as the sample sizes were not selected based on a predefined effect size. In this context, multiple experiments were independently performed, employing various sample replicates, as detailed in Table S5.

**Acknowledgments**

The authors would like to thank J. Andilla and M. Rivas for technical support and to the Lakadamyali lab for the Fiji plugin used to split data into ROIs. The research leading to these results has received funding from the European Commission H2020 Program under grant agreement ERC Adv788546 (NANO-MEMEC) (to M.F.G.-P.), Government of Spain (Severo Ochoa CEX2019-000910-S, State Research Agency (AEI) (PID2020-113068RB-I00 / 10.13039/501100011033 (to M.F.G.-P.), RYC-2017-22227 and PID2022-138282NB-I00 project funded by the MCIN/AEI/10.13039/501100011033/ FEDER, UE (to F.C.)), Fundació CELLEX (Barcelona), Fundació Mir-Puig and the Generalitat de Catalunya through the CERCA program and AGAUR (Grant No. 2021 SGR01450 M.F.G.-P.). N.M. acknowledges funding from the European Union H2020 under the Marie Sklodowska-Curie grant 754558-PREBIST.

## References


1. B. Geiger, J. P. Spatz, A. D. Bershadsky, Environmental sensing through focal adhesions. *Nat. Rev. Mol. Cell Biol.* **10**, 21–33 (2009).

2. J. D. Humphrey, E. R. Dufresne, M. A. Schwartz, Mechanotransduction and extracellular matrix homeostasis. *Nat. Rev. Mol. Cell Biol.* **15**, 802–812 (2014).

3. M. K. L. Han, J. De Rooij, Converging and Unique Mechanisms of Mechanotransduction at Adhesion Sites. *Trends Cell Biol.* **26**, 612–623 (2016).

4. K. A. Jansen, P. Atherton, C. Ballestrem, Mechanotransduction at the cell-matrix interface. *Semin. Cell Dev. Biol.* **71**, 75–83 (2017).

5. P. Roca-Cusachs, N. C. Gauthier, A. Del Rio, M. P. Sheetz, Clustering of α5β1 integrins determines adhesion strength whereas αvβ3 and talin enable mechanotransduction. *Proc. Natl. Acad. Sci. U. S. A.* **106**, 16245–16250 (2009).

6. A. Elosegui-Artola, *et al.*, Mechanical regulation of a molecular clutch defines force transmission and transduction in response to matrix rigidity. *Nat. Cell Biol.* **18**, 540–548 (2016).

7. C. T. Mierke, Bidirectional Mechanical Response Between Cells and Their Microenvironment. *Front. Phys.* **9**, 1–40 (2021).

8. N. D. Gallant, K. E. Michael, A. J. García, Cell Adhesion Strengthening: Contributions of Adhesive Area, Integrin Binding, and Focal Adhesion Assembly. *Mol. Biol. Cell* **16**, 4329–4340 (2005).

9. J. D. Humphries, *et al.*, Vinculin controls focal adhesion formation by direct interactions with talin and actin. *J. Cell Biol.* **179**, 1043–1057 (2007).

10. A. Elosegui-Artola, *et al.*, Rigidity sensing and adaptation through regulation of integrin types. *Nat. Mater.* **13**, 631–637 (2014).

11. N. Strohmeyer, M. Bharadwaj, M. Costell, R. Fässler, D. J. Müller, Fibronectin-bound α5β1 integrins sense load and signal to reinforce adhesion in less than a second. *Nat. Mater.* **16**, 1262–1270 (2017).

12. Y. L. Hu, *et al.*, FAK and paxillin dynamics at focal adhesions in the protrusions of migrating cells. *Sci. Rep.* **4**, 1–7 (2014).

13. C. Egles, *et al.*, Integrin-Blocking antibodies delay Keratinocyte Re-Epithelialization in a Human three-dimensional wound healing model. *PLoS One* **5**, 2–9 (2010).

14. G. Neiman, *et al.*, Integrin alpha-5 subunit is critical for the early stages of human pluripotent stem cell cardiac differentiation. *Sci. Rep.* **9**, 1–10 (2019).

15. J. L. Walker, R. K. Assoian, Integrin-dependent signal transduction regulating cyclin D1 expression and G1 phase cell cycle progression. *Cancer Metastasis Rev.* **24**, 383–393 (2005).

572 16. R. Pytela, M. D. Pierschbacher, E. Ruoslahti, Identification and isolation of a 140 kd
573 cell surface glycoprotein with properties expected of a fibronectin receptor. *Cell* **40**,
574 191–198 (1985).

575 17. I. F. Charo, L. Nannizzi, J. W. Smith, D. A. Cheresh, The vitronectin receptor α(v)β3
576 bind fibronectin and acts in concert with α5β1 in promoting cellular attachment and
577 spreading on fibronectin. *J. Cell Biol.* **111**, 2795–2800 (1990).

578 18. E. Ruoslahti, RGD and other recognition sequences for integrins. *Annu. Rev. Cell Dev.*
579 *Biol.* **12**, 697–715 (1996).

580 19. B. Geiger, E. Zamir, Molecular complexity and dynamics of cell-matrix adhesions. *J.*
581 *Cell Sci.* **114**, 3577–3579 (2001).

582 20. R. Zaidel-Bar, C. Ballestrem, Z. Kam, B. Geiger, Early molecular events in the assembly
583 of matrix adhesions at the leading edge of migrating cells. *J. Cell Sci.* **116**, 4605–4613
584 (2003).

585 21. R. Zaidel-Bar, S. Itzkovitz, A. Ma'ayan, R. Iyengar, B. Geiger, Functional atlas of the
586 integrin adhesome. *Nat. Cell Biol.* **9**, 858–867 (2007).

587 22. B. Geiger, K. M. Yamada, Molecular architecture and function of matrix adhesions.
588 *Cold Spring Harb. Perspect. Biol.* **3**, 1–21 (2011).

589 23. E. R. Horton, *et al.*, Definition of a consensus integrin adhesome and its dynamics during
590 adhesion complex assembly and disassembly. *Nat. Cell Biol.* **17**, 1577–1587 (2015).

591 24. J. D. Humphries, M. R. Chastney, J. A. Askari, M. J. Humphries, Signal transduction
592 via integrin adhesion complexes. *Curr. Opin. Cell Biol.* **56**, 14–21 (2019).

593 25. B. Z. Katz, *et al.*, Physical state of the extracellular matrix regulates the structure and
594 molecular composition of cell-matrix adhesions. *Mol. Biol. Cell* **11**, 1047–1060 (2000).

595 26. S. Seetharaman, S. Etienne-Manneville, Integrin diversity brings specificity in
596 mechanotransduction. *Biol. Cell* **110**, 49–64 (2018).

597 27. O. Rossier, *et al.*, Integrins β1 and β3 exhibit distinct dynamic nanoscale organizations
598 inside focal adhesions. *Nat. Cell Biol.* **14**, 1057–1067 (2012).

599 28. F. Kong, A. J. García, A. P. Mould, M. J. Humphries, C. Zhu, Demonstration of catch
600 bonds between an integrin and its ligand. *J. Cell Biol.* **185**, 1275–1284 (2009).

601 29. Y. Chen, H. Lee, H. Tong, M. Schwartz, C. Zhu, Force regulated conformational change
602 of integrin αVβ3. *Matrix Biol.* **60**–**61**, 70–85 (2017).

603 30. S. Huveneers, E. H. J. Danen, Adhesion signaling - Crosstalk between integrins, Src and
604 Rho. *J. Cell Sci.* **122**, 1059–1069 (2009).

605 31. H. B. Schiller, *et al.*, β1- and αv-class integrins cooperate to regulate myosin II during
606 rigidity sensing of fibronectin-based microenvironments. *Nat. Cell Biol.* **15**, 625–636
607 (2013).

32. C. Diaz, S. Neubauer, F. Rechenmacher, H. Kessler, D. Missirlis, Recruitment of αvβ3 integrin to α5β1 integrin-induced clusters enables focal adhesion maturation and cell spreading. *J. Cell Sci.* **133** (2020).

33. O. Rossier, G. Giannone, The journey of integrins and partners in a complex interactions landscape studied by super-resolution microscopy and single protein tracking. *Exp. Cell Res.* **343**, 28–34 (2016).

34. T. Orré, O. Rossier, G. Giannone, The inner life of integrin adhesion sites: From single molecules to functional macromolecular complexes. *Exp. Cell Res.* **379**, 235–244 (2019).

35. P. Kanchanawong, *et al.*, Nanoscale architecture of integrin-based cell adhesions. *Nature* **468**, 580–584 (2010).

36. E. Betzig, *et al.*, Imaging intracellular fluorescent proteins at nanometer resolution. *Science (80-. ).* **313**, 1642–1645 (2006).

37. R. Changede, X. Xu, F. Margadant, M. P. Sheetz, Nascent Integrin Adhesions Form on All Matrix Rigidities after Integrin Activation. *Dev. Cell* **35**, 614–621 (2015).

38. M. Spiess, *et al.*, Active and inactive β1 integrins segregate into distinct nanoclusters in focal adhesions. *J. Cell Biol.* **217**, 1929–1940 (2018).

39. T. K. Fujiwara, *et al.*, Ultrafast single-molecule imaging reveals focal adhesion nano-architecture and molecular dynamics. **222** (2023).

40. A. C. Chang, *et al.*, Single Molecule Force Measurements in Living Cells Reveal a Minimally Tensioned Integrin State. *ACS Nano* **10**, 10745–10752 (2016).

41. S. J. Tan, *et al.*, Regulation and dynamics of force transmission at individual cell-matrix adhesion bonds. *Sci. Adv.* **6**, 1–12 (2020).

42. M. Ester, H. P. Kriegel, J. Sander, X. Xu, A Density-Based Algorithm for Discovering Clusters in Large Spatial Databases with Noise. *AAAI Press*, 226–231 (1996).

43. M. J. Rust, M. Bates, X. Zhuang, Sub-diffraction-limit imaging by stochastic optical reconstruction microscopy (STORM). *Nat. Methods* **3**, 793–796 (2006).

44. S. V. Pageon, P. R. Nicovich, M. Mollazade, T. Tabarin, K. Gaus, Clus-DoC: A combined cluster detection and colocalization analysis for single-molecule localization microscopy data. *Mol. Biol. Cell* **27**, 3627–3636 (2016).

45. P. Kanchanawong, D. A. Calderwood, Organization, dynamics and mechanoregulation of integrin-mediated cell–ECM adhesions. *Nat. Rev. Mol. Cell Biol.* **0123456789** (2022).

46. S. Tadokoro, *et al.*, Talin binding to integrin β tails: A final common step in integrin activation. *Science (80-. ).* **302**, 103–106 (2003).

47. P. Atherton, *et al.*, Relief of talin autoinhibition triggers a force-independent association with vinculin. *J. Cell Biol.* **219** (2020).

644 48. N. C. Gauthier, P. Roca-Cusachs, Mechanosensing at integrin-mediated cell–matrix
645 adhesions: from molecular to integrated mechanisms. *Curr. Opin. Cell Biol.* **50**, 20–26
646 (2018).

647 49. P. Atherton, *et al.*, Tensin3 interaction with talin drives the formation of fibronectin-
648 associated fibrillar adhesions. *J. Cell Biol.* **221** (2022).

649 50. I. Thievessen, *et al.*, Vinculin-actin interaction couples actin retrograde flow to focal
650 adhesions, but is dispensable for focal adhesion growth. *J. Cell Biol.* **202**, 163–177
651 (2013).

652 51. T. S. van Zanten, *et al.*, Hotspots of GPI-anchored proteins and integrin nanoclusters
653 function as nucleation sites for cell adhesion. *Proc. Natl. Acad. Sci. U. S. A.* **106**, 18557–
654 18562 (2009).

655 52. A. Cambi, *et al.*, Organization of the Integrin LFA-1 in Nanoclusters Regulates Its
656 Activity. *Mol. Biol. Cell* **17**, 4270–4281 (2006).

657 53. S. J. Han, *et al.*, Pre-complexation of talin and vinculin without tension is required for
658 efficient nascent adhesion maturation. *Elife* **10**, 1–29 (2021).

659 54. J. C. Friedland, M. H. Lee, D. Boettiger, Mechanically activated integrin switch controls
660 α5β 1 function. *Science (80-. ).* **323**, 642–644 (2009).

661 55. Z. Sun, *et al.*, Kank2 activates talin, reduces force transduction across integrins and
662 induces central adhesion formation. *Nat. Cell Biol.* **18**, 941–953 (2016).

663 56. B. P. Bouchet, *et al.*, Talin-KANK1 interaction controls the recruitment of cortical
664 microtubule stabilizing complexes to focal adhesions. *Elife* **5**, 1–23 (2016).

665 57. K. Guo, *et al.*, KANK1 shapes focal adhesions by orchestrating protein binding,
666 mechanical force sensing, and phase separation. *Cell Rep.* **42**, 113321 (2023).

667 58. L. B. Case, M. De Pasquale, L. Henry, M. K. Rosen, Synergistic phase separation of two
668 pathways promotes integrin clustering and nascent adhesion formation. *Elife* **11**, 1–36
669 (2022).

670 59. B. Huang, W. Wang, M. Bates, X. Zhuang, SOM_Three-dimensional super-resolution
671 imaging by stochastic optical reconstruction microscopy. *Science (80-. ).* **319**, 810–813
672 (2008).

673 60. A. Dani, B. Huang, J. Bergan, C. Dulac, X. Zhuang, Superresolution Imaging of
674 Chemical Synapses in the Brain. *Neuron* **68**, 843–856 (2010).

675 61. M. Lelek, *et al.*, Single-molecule localization microscopy. *Nat. Rev. Methods Prim.* **1**
676 (2021).

677 62. J. Schindelin, *et al.*, Fiji: An open-source platform for biological-image analysis. *Nat.
678 Methods* **9**, 676–682 (2012).

679

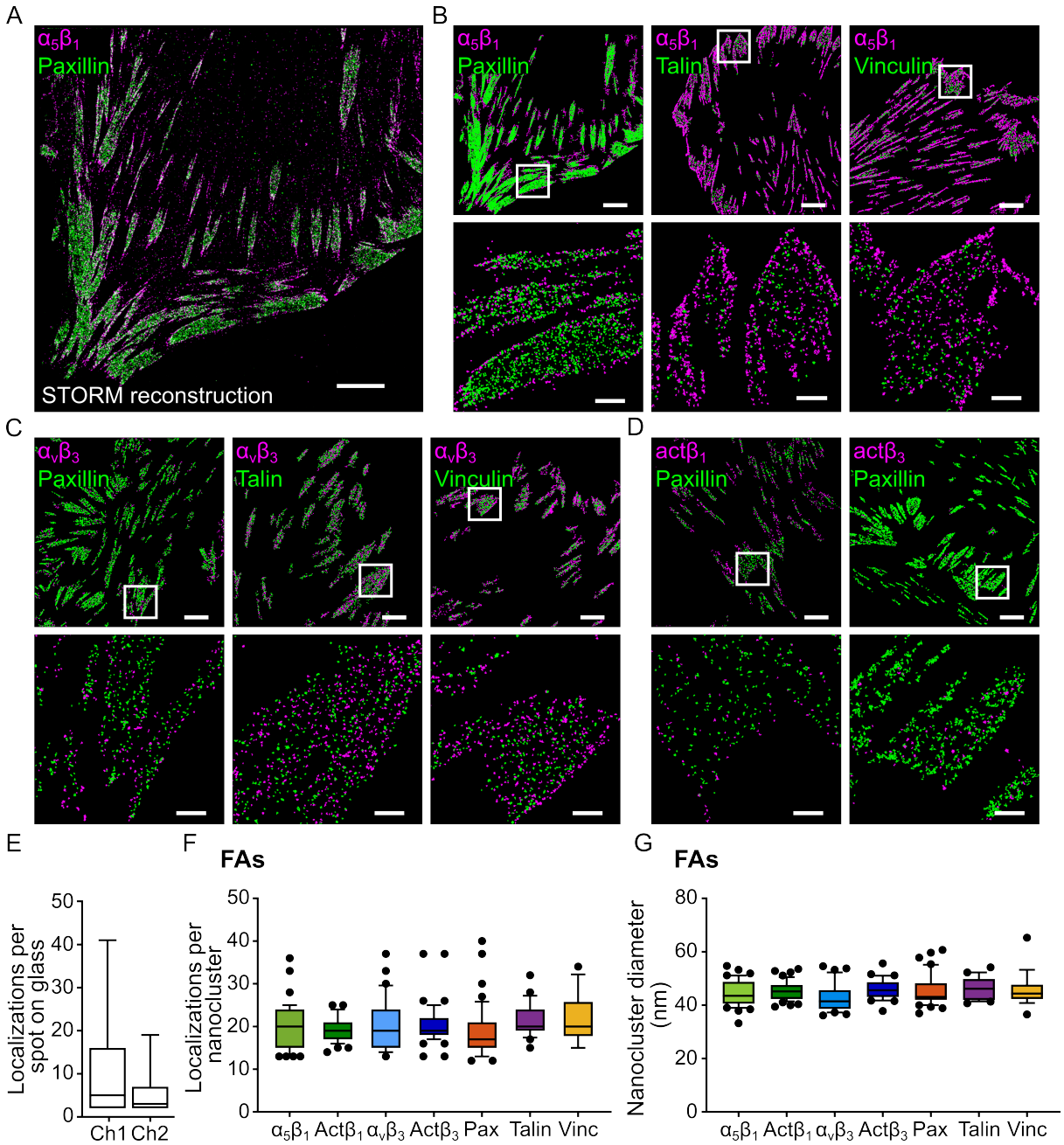


**Figure 1 Proteins of FAs organize as universal nanoclusters of similar size and containing a similar number of proteins.**

(A) Representative dual-color STORM image of an HFF-1 cell fixed after 24 h on FN and labeled for $\alpha_5\beta_1$ (magenta) and paxillin (green). Scale bar: 5 µm. (B) Representative images of all the adhesions identified for $\alpha_5\beta_1$ with paxillin (left), talin (middle) and vinculin (right), with zoomed-in regions shown below each panel. Scale bar top row: 5 µm, bottom row: 1 µm. (C) Representative images of all the adhesions identified for $\alpha_v\beta_3$ with paxillin (left), talin (middle)

688 and vinculin (right), with zoomed-in regions shown below each panel. Scale bar top row: 5 μm,
689 bottom row: 1 μm. (D) Representative images all the adhesions identified for of active $\alpha_5\beta_1$
690 (act$\beta_1$) with paxillin (left), active $\alpha_v\beta_3$ (act$\beta_3$) with paxillin (right), with zoomed-in regions
691 shown below each panel. Scale bar top row: 5 μm, bottom row: 1 μm. (E) Distribution for the
692 number of localizations per secondary antibody on glass next to cell regions for both of the
693 secondary antibodies used in this study, goat anti-mouse Alexa 405–Alexa 647 (Ch1) and goat
694 anti-rabbit Cy3–Alexa 647 (Ch2). The median number of localizations per spot corresponds
695 to: 5 for Alexa 405-Alexa 647-conjugated antibodies and 3 for Cy3–Alexa 647-conjugated
696 antibodies (see Materials & Methods). (F,G) Box-and-whisker plots showing the number of
697 localizations per nanocluster (F) and the nanocluster diameter (G) for the proteins in this study.
698 Each data point corresponds to the median value over all nanoclusters for each cell (for N
699 values, i.e., number of independent experiments, see SI Table S5). No statistical differences
700 were found using the one-way ANOVA test, where not significant (ns) corresponds to $p>0.05$.

701

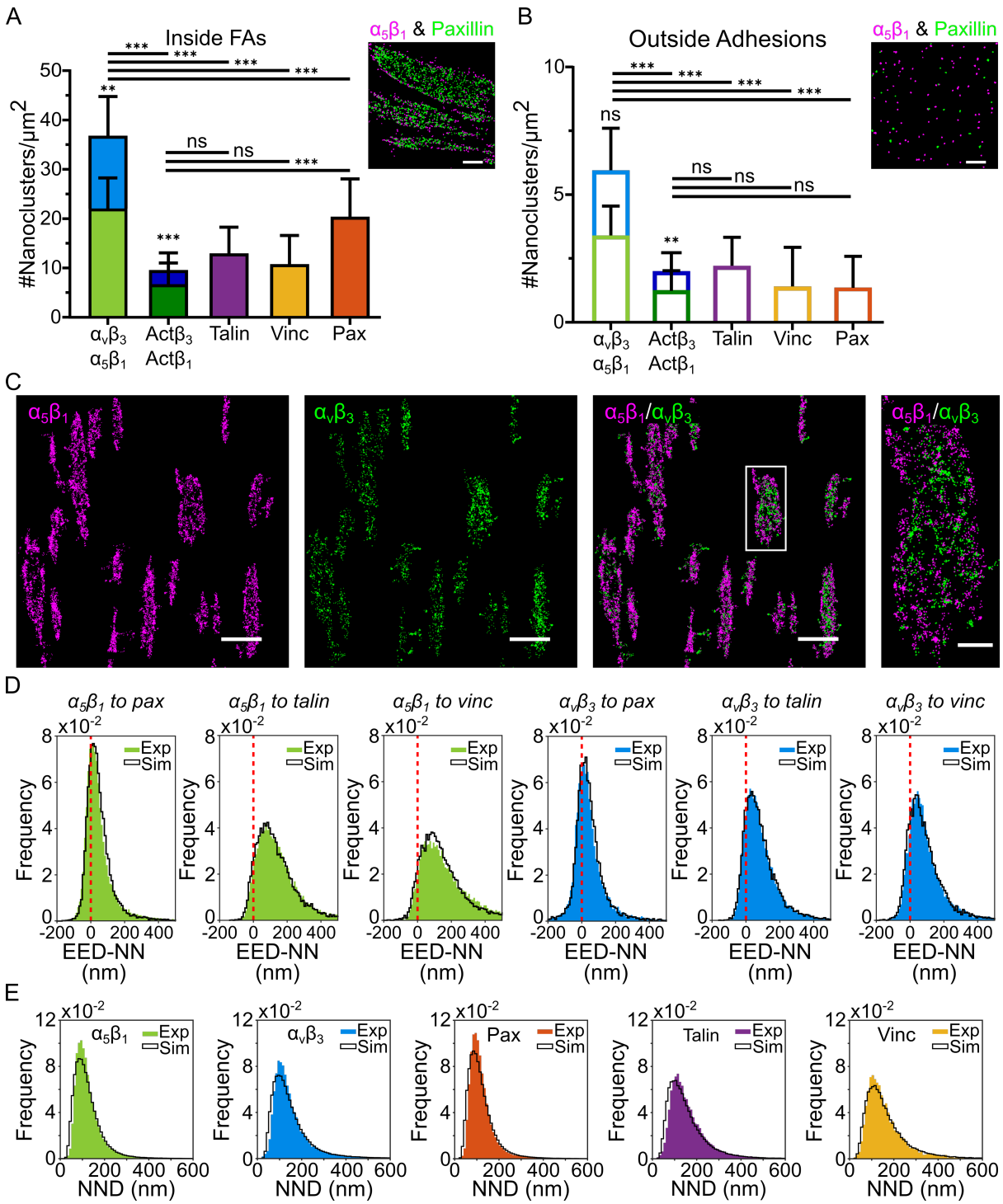


**Figure 2 Mesoscale organization of integrin nanoclusters and adaptor proteins inside FAs.** (A,B) Mean density of nanoclusters per unit area inside FAs (A) and on the cell membrane outside adhesions (B). The densities of integrins nanoclusters per unit area are shown as stacked graphs to allow comparison between the total number of integrin nanoclusters ($\alpha_5\beta_1$ and $\alpha_v\beta_3$) and the adaptor proteins. Statistical significance between data of all proteins was tested using

708 a one-way ANOVA and the comparison between $\alpha_5\beta_1$ and $\alpha_v\beta_3$, (act$\beta_1$ and act$\beta_3$) was done
709 with an unpaired t-test, where ns = not significant, $p>0.05$; *, $p<0.05$; **, $p<0.01$; ***, $p<0.001$.
710 The insets show representative images of nanoclusters for $\alpha_5\beta_1$ (magenta) and paxillin (green)
711 in FAs (A) and outside adhesions (B). Scale bar: 1 μm. (C) Representative dual-color STORM
712 image of the total populations of $\alpha_5\beta_1$ (magenta) and $\alpha_v\beta_3$ (green) integrins inside FAs. The
713 panel on the far-right side corresponds to a zoomed-in region of a single FA (white box)
714 showing spatially segregated $\alpha_5\beta_1$ and $\alpha_v\beta_3$ nanoclusters. Scale bars: 2 μm, and 500 nm for the
715 zoomed-in region. (D) Histogram of the EED-NN values between $\alpha_5\beta_1$ and the different
716 adaptors (green) and, between $\alpha_v\beta_3$ and the adaptors (blue). The black line in each plot
717 corresponds to the histogram for the simulated data sets. The dashed red line at zero
718 corresponds to nanoclusters contiguous to each other. Percentage of overlapping nanoclusters:
719 $\alpha_5\beta_1$-paxillin: exp = 28.4%, sim = 24.4%; $\alpha_5\beta_1$-talin: exp = 6.7%, sim = 8.1%; $\alpha_5\beta_1$-vinculin:
720 exp = 6.0%, sim = 7.7%; $\alpha_v\beta_3$ -paxillin: exp =31.7%, sim=29.2%; $\alpha_v\beta_3$ -talin: exp =15.7%,
721 sim=16.5; $\alpha_v\beta_3$-vinculin: exp =14.9%, sim=17.4%. (E) Histogram of the NND values between
722 nanoclusters of the same protein. The black line in each plot corresponds to the histogram for
723 the simulated data sets. Bin width is 10 nm.

724

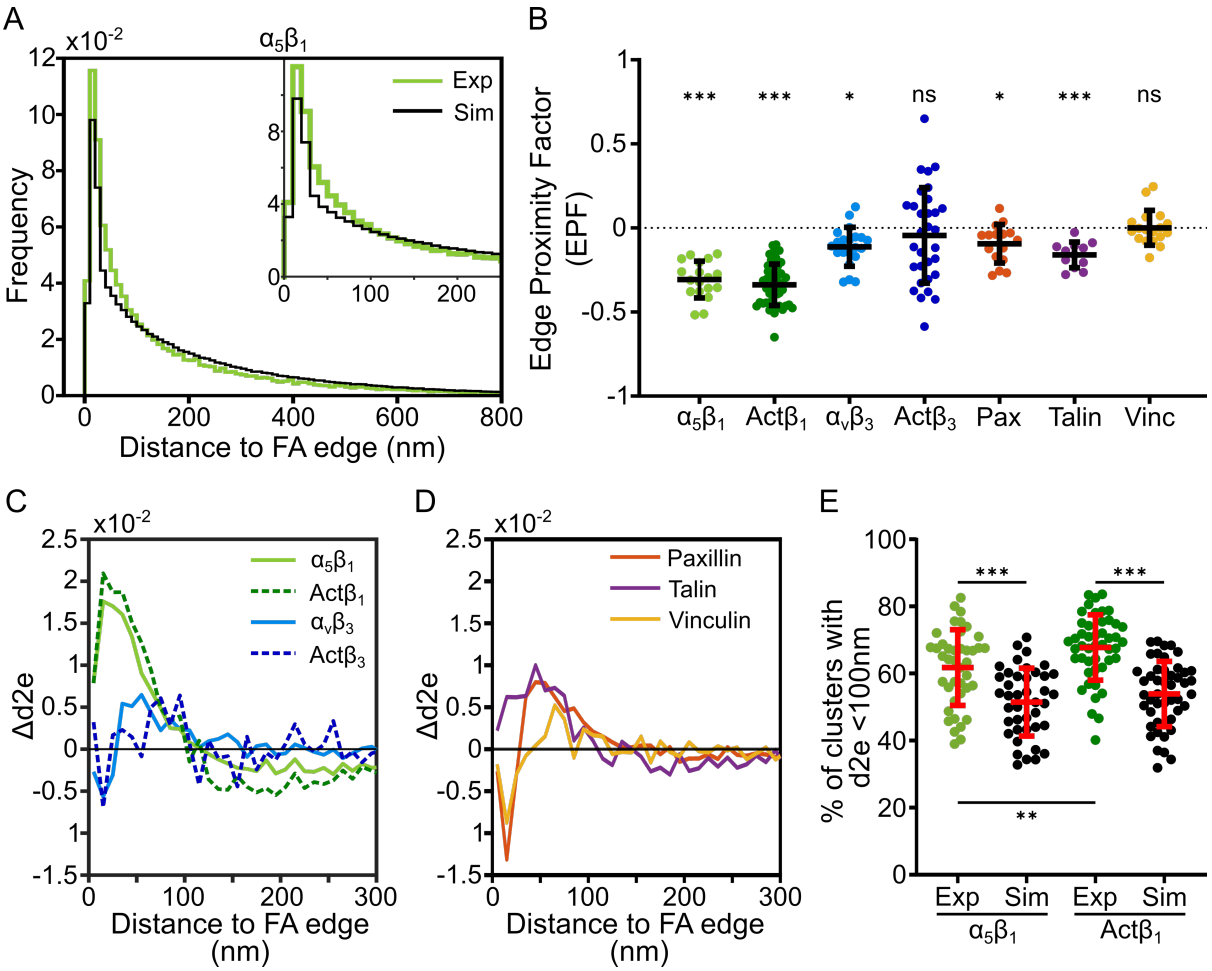


**Figure 3 Integrin $\alpha_5\beta_1$ nanoclusters are preferentially distributed on the edges of FAs.** (A) Distribution of distances from the center of mass (CoM) position of each individual $\alpha_5\beta_1$ nanocluster to its closest FA edge obtained from DBSCAN-analyzed STORM images. The histogram represents the frequency distribution over all cells. Green lines correspond to the experimental data (Exp) and the simulated uniform distribution (Sim) is shown as a black histogram. Bin width is 10 nm. The inset shows the distribution for the first 250 nm. (B) Edge Proximity Factor (EPF) per cell for each of the proteins investigated. Data are shown as individual median values per cell (color dots) together with the mean ± st. dev. superimposed in black. Statistical significance between experimental and simulated data was tested using a paired t-test, where ns = not significant, $p>0.05$; *, $p<0.05$; **, $p<0.01$; ***, $p<0.001$. (C,D) Deviation of the nanocluster distances from the FA edges with respect to random (Δd2e), as function of the distance to the FA edges for $\alpha_5\beta_1$ and $\alpha_v\beta_3$ integrin nanoclusters (C) and for the adaptor proteins (D). (E) Percentage of nanoclusters proximal to FA edges (<100nm) for the

739 total and active $\alpha_5\beta_1$ nanocluster population (color dots) together with results from simulations
740 of random organization (black dots). Each dot corresponds to the median value per cell, each
741 cell containing multiple FAs. Statistical significance between experimental and simulated data
742 was tested using a paired t-test, and to test the significance between $\alpha_5\beta_1$ and Act$\beta_1$ the unpaired
743 t-test was used, where ns = not significant, $p>0.05$; *, $p<0.05$; **, $p<0.01$; ***, $p<0.001$.

744

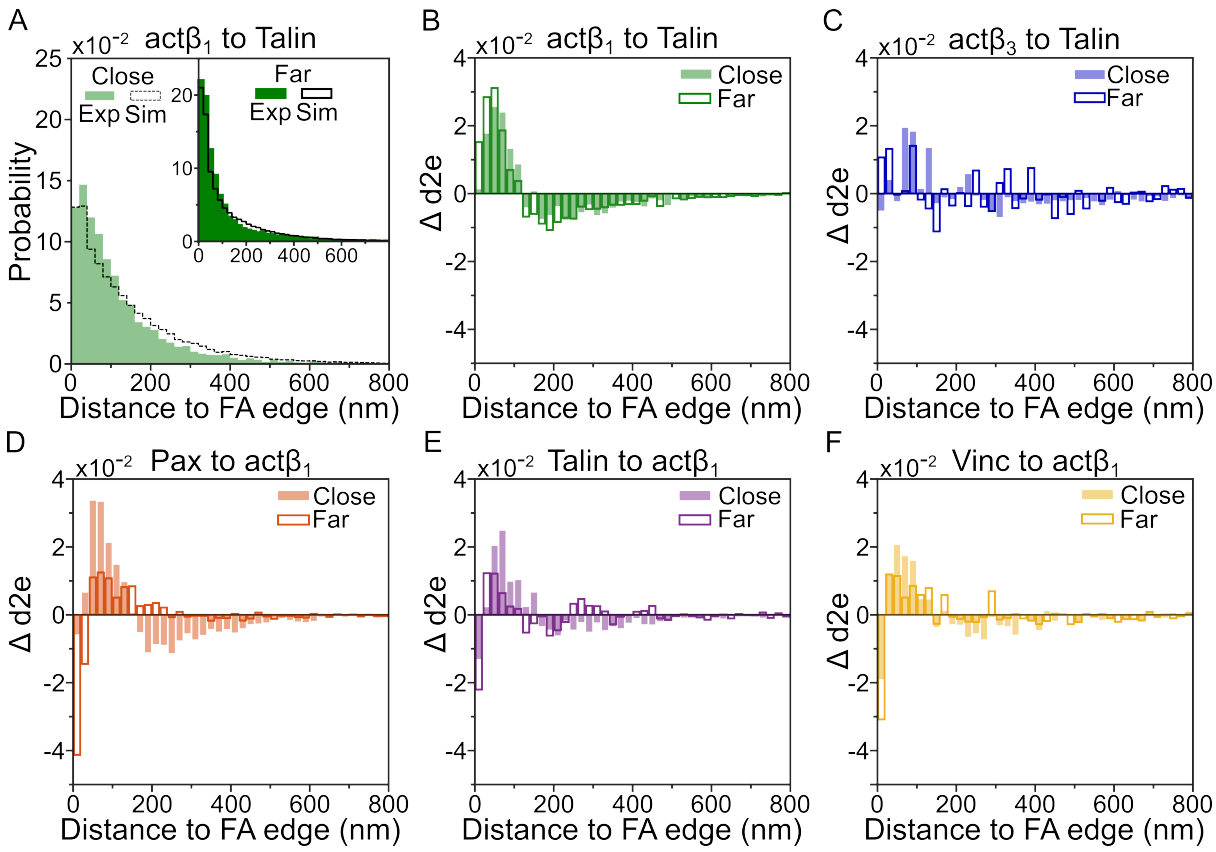


**Figure 4 Integrin $\alpha_5\beta_1$ forms multiprotein hubs at the FA edges**

(A) Distribution of distances to FA edge from data split depending on the *i*NND from act$\beta_1$ nanoclusters to talin. The data plotted in light green is the distance from CoM to FA edge for act$\beta_1$ nanoclusters with *i*NND < *Mdn,* while the inset dark green is the distance from CoM to FA edge for act$\beta_1$ nanoclusters with *i*NND > *Mdn.* Black lines are for simulated data sets. Bin width is 20 nm. (B-F) Δd2e-plots of the distance-to-edge for nanoclusters close to their partner NN, (*i*NND < *Mdn*, filled bar plots) and for nanoclusters far from their partner NN (*i*NND > *Mdn*; empty bar plots). (B,C) Distance-to-edge Δd2e-plots for act$\beta_1$ (B) and act$\beta_3$ (C) nanoclusters in FAs, considering their proximity to talin clusters. (D, E, F) Distance-to-edge Δd2e-plots for adaptor nanoclusters in FAs, paxillin (D), talin (E), vinculin (F), considering their proximity to act$\beta_1$ nanoclusters. Bin width is 20 nm.

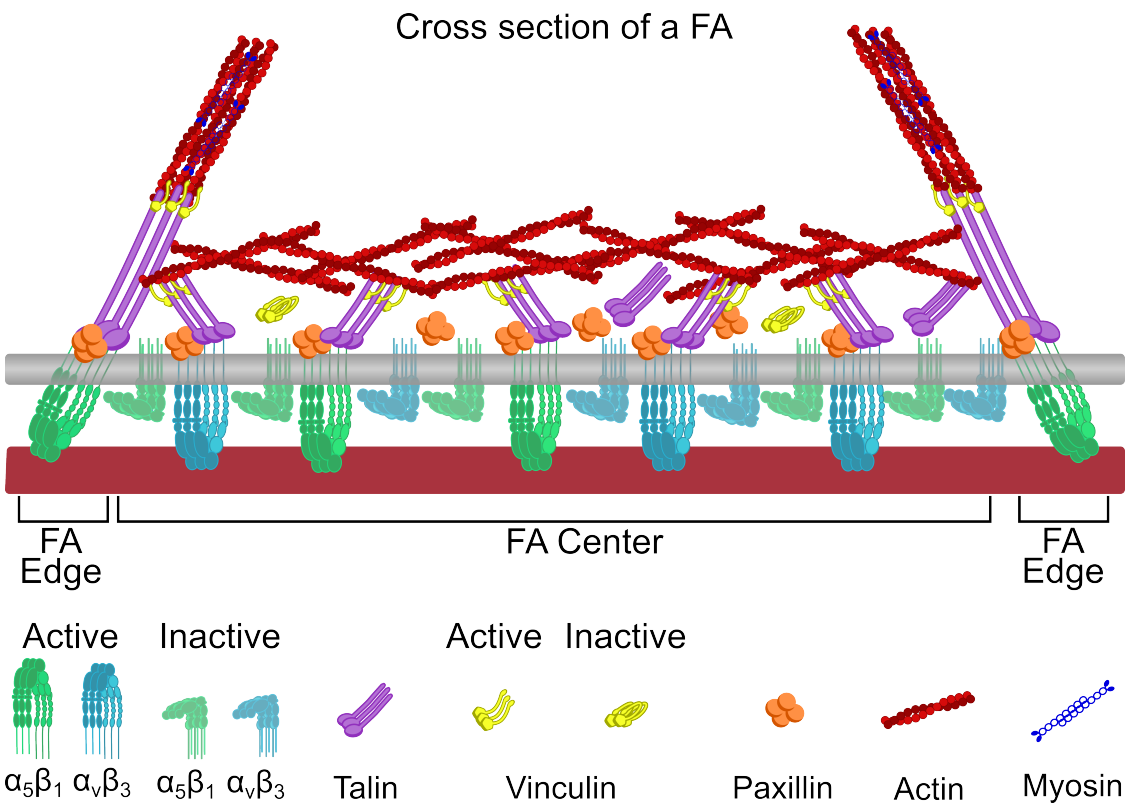


**Figure 5 Spatial regulation and activation of integrin nanoclusters and protein adaptors inside focal adhesions.**

$\alpha_5\beta_1$, $\alpha_v\beta_3$, and main protein adaptors organize as small nanoclusters inside FAs physically segregated from each other. A considerable high fraction of $\alpha_5\beta_1$ and $\alpha_v\beta_3$ integrins remain in an inactive state and do not intermix at the nanoscale. Active $\alpha_5\beta_1$ nanoclusters (green) on the FA edge reside in close proximity to the adaptor protein nanoclusters and thus possibly engaged to actomyosin filaments (red and blue). Integrin nanoclusters in the FA center are more randomly distributed with respect to one another, most probably engaged with branched cortical actin. According to our results we propose that $\alpha_5\beta_1$ nanoclusters located at the FA periphery could be primarily involved in cell substrate attachment, whereas $\alpha_5\beta_1$ and $\alpha_v\beta_3$ nanoclusters at the center of FAs engage in mechanosensing and mechanotransduction.